Influence of radiation-damage evolution on lattice-location measurements for Yb and Au in iron*

C. Cohen, F. Abel, and M. Bruneaux
Groupe de Physique des Solides de l'Ecole Normale Supérieure, Université Paris VII, 75221 Paris, France

L. Thomé and H. Bernas
Institut de Physique Nucléaire, Université Paris-Sud, 91406-Orsay, France

J. Chaumont
Laboratoire René-Bernas du Centre de Spectrométrie Nucléaire et de Spectrométrie de Masse, 91406 Orsay, France

(Received 22 May 1978)

The influence of radiation damage on the lattice location of heavy impurities (Yb and Au) implanted in iron is studied by channeling experiments. The nature of the impurity–radiation-damage interaction has been modified by annealing of room-temperature implanted samples or high-temperature implantation. The value of the corrected extinction ratio ϵ measured in several crystallographic directions on room-temperature implanted Yb and Au impurities cannot be interpreted uniquely in terms of different site populations. The annealing- and implantation-temperature dependences of the ratio ϵ for Yb-implanted Fe are very different. Upon annealing, the value of ϵ is unchanged up to 450 °C and then drops abruptly. In hot-implant experiments, the extinction ratio starts to fall at ~150 °C when vacancies become mobile. Vacancy-assisted diffusion is suggested to cause the changes of ϵ in both experiments. The temperature dependence of ϵ for the (100) plane is found to differ from that in other directions. This planar effect suggests that Yb impurities move preferentially in the (100) plane, which is the plane of vacancy loops in Fe. A quantitative analysis of these lattice-location results and of related hyperfine-interaction results is presented in a companion paper.

I. INTRODUCTION

This is the third in a series[1] of four papers on the correlation, pointed out[2–4] some time ago, between hyperfine-interaction (HFI) and lattice-location results on impurities implanted into Fe and Ni. This correlation has now[5–9] apparently been well substantiated, but its origin is still not understood. Two features hamper attempts at clarification. First, many of these experiments have been performed on implanted impurities that are chemically insoluble in Fe or Ni, so that it is difficult to obtain information on the properties of such alloys. A more basic problem is that since lattice-location experiments can in general only be carried out on near-surface atoms, ion implantation is practically the only means of sample preparation. This produces radiation damage, most of which overlaps the implanted-impurity depth distribution.[10] If the impurity interacts with the radiation damage, its lattice location is affected via crystal distortions and its HFI is modified via changes in the charge and spin distribution of the impurity electronic wave functions. The effect of radiation-damage evolution, due to sample annealing or high-temperature implantation, on the HFI of ^{169}Tm and ^{175}Lu in Fe was discussed in Paper II. Its effect on lattice-location studies of Yb and Au impurities in Fe is reported here. A more general discussion of impurity-damage interaction effects in HFI and lattice-location results for heavy impurities in metals is presented in Paper IV, which also offers a quantitative analysis that relates the HFI and lattice-location results.

II. EXPERIMENTAL

Most of our experimental techniques have been described or referred to previously. Here, we only report new material pertinent to the present experiments.

A. Samples

The impurity content of our monocrystalline iron samples amounted to approximately 400 ppm (mostly light impurities, including 20 ppm oxygen). The orientation of the samples was very near to (001). Standard annealing and electropolishing operations[11] were performed before ion implantation. After polishing, the oxygen content of the remaining oxide layer was measured on several test samples, via the ^{16}O$(d,p)^{17}$O* nuclear reaction,[12] and found to be

 ©1979 The American Physical Society

about 10^{16} atoms cm^{-2} (corresponding to an oxide layer of approximately 30 Å assuming Fe_2O_3).

B. Implantation and sample-annealing treatments

The Orsay ion implantor, on which implantations were performed, is a 50-kV high-current machine equipped with a 90-kV post-accelerating lens whose main features have been described elsewhere.[13] Neutral particles are eliminated; ion beam currents are measured using a digital current integrator and a secondary electron repeller. The precision on the implanted dose measurement is better than 5%, as checked by the Rutherford backscattering experiments themselves. Because of the high-current capabilities of the ion source, implantations may be performed at energies up to 400 keV using triply charged ion beams with currents up to ~1.0 μA. This feature was of major importance in the present work: the implantation had to be deep enough to avoid any interaction of the implanted atoms with the sample surface (especially the surface oxide layer).

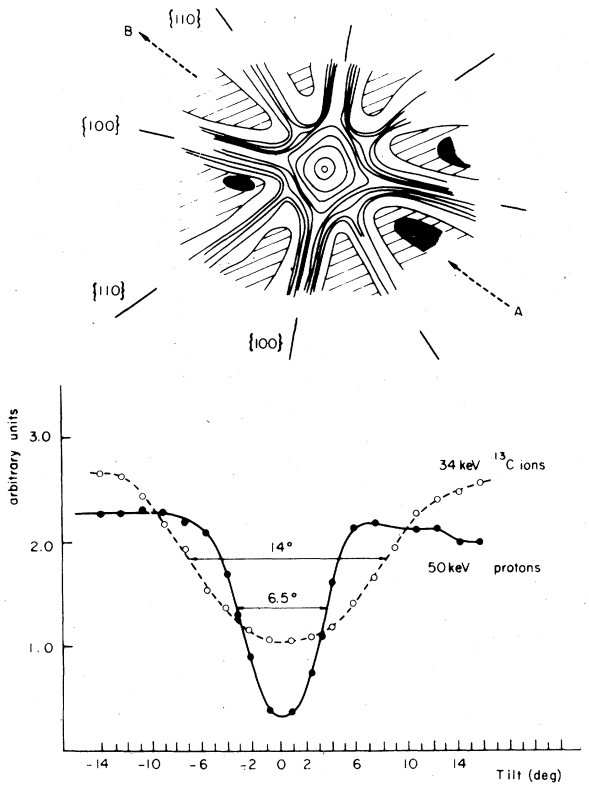

FIG. 1. Isocurrent curves and angular scans across the [100] axis, obtained in the implantor on Fe crystals (see text). The direction *A-B* along which the scans are performed is indicated in the upper part of the figure. Angular scans: full line, 50-keV protons; dashed line, 34-keV ^{13}C ions.

As discussed below, interesting comparisons were possible with previous experiments performed at lower energies.

The iron single crystals were mounted on a goniometer and aligned in the implantor itself via the channeling technique by measuring the change in current on the secondary electron repeller, due mostly to backscattered particles, as the sample was tilted. A typical result is presented in Fig. 1. In the upper part (incoming 50-keV protons), the isocurrent curves are mapped out around the (001) axis (perpendicular to the page), and the main planes are clearly seen. A cut across this figure (along *AB*) produces the characteristic angular scan displayed in the lower part of Fig. 1. The width of the angular scan for 34-keV ^{13}C ions (also shown in Fig. 1) is exactly what one expects for 400-keV Yb ions from Ref. 14. Special care was exercised in order to avoid channeling in "random-implantation" experiments.

For the high-temperature implants, the sample was mounted on a small heater on the rotation axis of the goniometer.[13]

Room-temperature implanted samples were annealed in an ion-pump vacuum furnace with a liquid-nitrogen trap: the vacuum was better than 10^{-7} Torr.

C. Lattice-location experiments

Our lattice-location experiments were performed using the 2-MeV Van de Graaff accelerator of the Groupe de Physique des Solides de l'Ecole Normale Supérieure and the beam handling system described in Ref. 15. The goniometric chamber, described elsewhere,[16] allows rotation of the sample around three axes crossing at the impact position of the analyzing beam on the sample surface. The rotations are driven by stepping motors. Samples may be translated in their own plane without significant misalignment (less than 1'); this is necessary in order to avoid damage effects induced by high doses of the probing beam on a given impact point. A vacuum of $\sim 5 \times 10^{-7}$ Torr is obtained in the chamber by means of a diffusion pump and a liquid-nitrogen trap.

Our experiments were performed using 1.8-MeV ^{14}N ions. Similar beams were used in other[9,17,18] lattice-location experiments, but they have disadvantages such as radiation damage to the sample or to the detector. It is therefore useful to justify their use here. Basically, our experiments compare the backscattering yield (as a function of depth) on host atoms and on the small amount of heavy impurity-implanted atoms. Three parameters have to be taken into account: mass separation, depth resolution, and sensitivity. Very-light-ion probing beams are inadequate owing to the low values of the stopping power and to the small variation of the kinematic coefficient

with the target atom mass. The choice then lies between ^{4}He and heavier ions such as ^{12}C, ^{14}N, or ^{16}O. It has been shown[19] that between 1 and 2 MeV, the mass separation and depth resolution obtained with these particles are essentially equal, as the higher stopping power and the sharper variation of the kinematic coefficient with target mass atoms for heavier particles are almost exactly compensated by the poorer energy resolution obtained with surface-barrier detectors for these ions. In our experiments, the main advantage of ^{12}C, ^{14}N, or ^{16}O beams, as compared to ^{4}He, was the gain in sensitivity. Pulse pile-up problems play an essential role here. It is known that the amount of pile-up is governed by the *ratio* of the pulse amplitudes, and that the pile-up intensity is drastically reduced when the amplitude ratio increases even slightly. Since the ratios of the energies E of backscattered particles on ^{174}Yb and ^{56}Fe are respectively 1.2 for ^{4}He and 2.0 for ^{14}N ions, ^{14}N ions are clearly more effective than ^{4}He ions for our experiments. The beam energy was chosen by noting that mass separation is energy proportional, and that for ^{14}N ions, the depth resolution improves with energy in our energy range (the stopping power increasing like $E^{1/2}$ and the energy resolution varying[20] like $E^{1/3}$).

Backscattered particles were analyzed with surface-barrier detectors (area 25 mm^2, resistivity $\sim$1000 Ω cm). The solid angle of detection was $\sim 10^{-3}$ sr and the backscattering angle 165°. The data-acquisition system was conventional, except that pulse pile-up was again minimized by using a fast, voltage-sensitive, nanosecond amplifier[21] with a rise time of about 8 ns. The system can handle millions of background counts per second without overload: pile-up in the analysis of higher amplitudes is determined only by the pulse-clipping time (10 ns). A peak value stretcher with a variable threshold restricts the analysis to the less numerous high-amplitude pulses, while background pulses are eliminated. The typical noise of our electronics was equivalent to 45 keV (FWHM), a value that would affect the energy and depth resolution drastically if ^{4}He beams were used. But owing to the poor energy resolution already obtained with low-noise systems for ^{14}N beams, the use of fast electronics only leads to an energy-resolution increase of $\sim$50% in our case, i.e., to measured values of 70 keV which correspond to a depth resolution of 180 Å in iron (assuming "random" stopping power for the energy-to-depth conversion). Typical results obtained in our experimental conditions (probing beam current typically 100 nA; integrated charge typically 30 μC) are illustrated in Fig. 2. The height of the Yb peak is $\sim$2% of the Fe edge. The energy calibration of the recorded spectra is of prime importance for data reduction. For various reasons (elastic energy-loss processes, electron-hole recombination, etc.), the response of the surface-barrier detector to ^{14}N ions is not exactly energy proportional. A study of the pulse height defect as a function of particle energy is thus required. Our energy calibration includes the results[22] of such a study, performed under conditions similar to ours. Frequent checking of pulse amplitude changes due to the radiation damage induced by the backscattered ^{14}N ions in the surface-barrier detector was also found to be necessary.

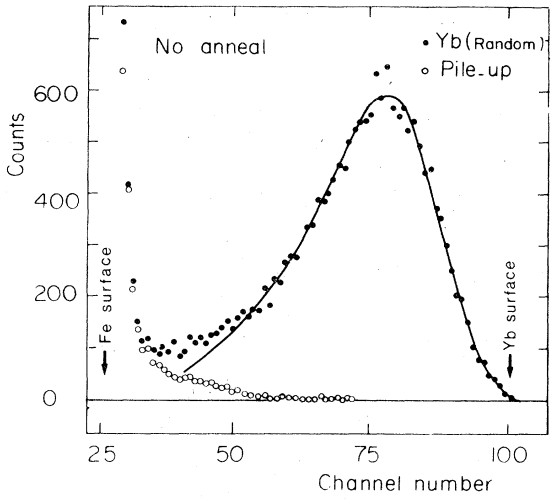

FIG. 2. Random backscattering spectrum on an Fe crystal implanted with 5×10^{14} Yb atoms/cm^2 at 400 keV in a random direction (full circles). Comparison with a random spectrum obtained in identical conditions on an unimplanted sample (open circles) provides an estimate of the very low pile-up contribution. Calibration: 7 keV/channel. Full line is a fit to the experimental profile (see text).

III. DATA REDUCTION

A. Measured parameters

The important parameter extracted from the data is the corrected extinction ratio $\epsilon(x)$ which can be defined, for a given direction of the probing beam, as

$$\epsilon(x) = \frac{1-\chi_i(x)}{1-\chi_h(x)} \quad , \tag{1}$$

where $\chi_i(x)$ and $\chi_h(x)$ are the backscattering yields at depth x (normalized to the respective random yields at the same depth) for the impurity and for the host. In a simple interpretation, the fraction of impurities occupying specific lattice sites is obtained by measuring ϵ along various crystallographic directions. This interpretation ignores the influence of lattice defects, and will be discussed in Paper IV.

In experiments on low-energy implants, the impur-

ity profile is narrow compared to the depth resolution and the only available parameter is the mean value $\bar{\epsilon}$ averaged over the whole impurity profile. The numerator of Eq. (1) is then obtained from the ratio of the integral of the impurity peaks in aligned and random spectra. However, since the stopping power of a channeled particle depends on its transverse energy, there is no well-defined energy-to-depth conversion for energy spectra in aligned directions. The exact value of χ_h in the denominator of Eq. (1) is thus uncertain. This difficulty is negligible when channeling is studied in directions corresponding to major crystallographic axes; χ_h is then very small compared to unity. The denominator of Eq. (1) is then very close to 1 and uncertainties in χ_h do not lead to significant errors in $\bar{\epsilon}$. The problem is crucial in planar channeling experiments where χ_h varies steeply with depth. Then, changes in the energy-to-depth conversion scale lead to large variations of the normalizing term $1-\chi_h$ of Eq. (1) and hence to large variations of $\bar{\epsilon}$. In the present experiments, the width and energy position of the Yb peak were found to be very similar for spectra taken in random or in planar aligned directions. This is a strong indication that the random stopping power should be used for the energy-to-depth conversion in planar channeling backscattering experiments, a result confirmed by various other planar channeling experiments. In our analysis, we have always used the random stopping power as evaluated by interpolation from the data[23] for Ni and Ti.

In the experiments performed here on 400 keV implants, the impurity depth profile is broad compared to the depth resolution. In principle, it is then possible to determine the depth dependence of ϵ. This would provide information in the consequences of impurity, and damage, distribution overlap. However, the overall variation of $\epsilon(x)$ was found to be of the order of the uncertainties due to the energy to depth conversion. Thus, except in the aligned implantation spectra (Sec. IV C), no attempt was made to derive the depth dependence of ϵ. Henceforth, our results are all presented in terms of $\bar{\epsilon}$ and we shall omit the bar for convenience.

B. Determination of the implantation profiles

For an implantation energy of 400 keV, the implantation profile is wide compared to the depth resolution of backscattering experiments, and may be obtained by analyzing the random backscattering spectra. Profiles corresponding to implantations performed in a random direction were determined using a program[22] developed by A. L'Hoir. Typical fits are presented in Figs. 2 and 3 for 400-keV Yb and Au implants. The corresponding depth profiles are compared to theoretical predictions[24] in Fig. 4 and the re-

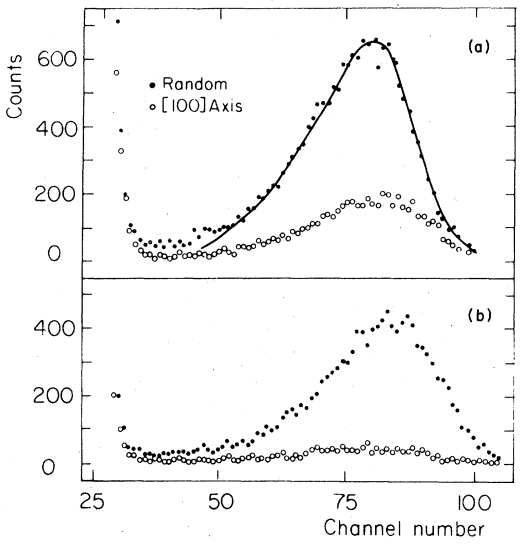

FIG. 3. Random and [100] aligned backscattering spectra on Fe crystals implanted at RT with 5×10^{14} Au atoms/cm^2 at 400 keV: (a) unannealed sample, (b) 500 °C annealed sample. Calibration: 8.2 keV/channel. Full line is a fit to the experimental profile (see text).

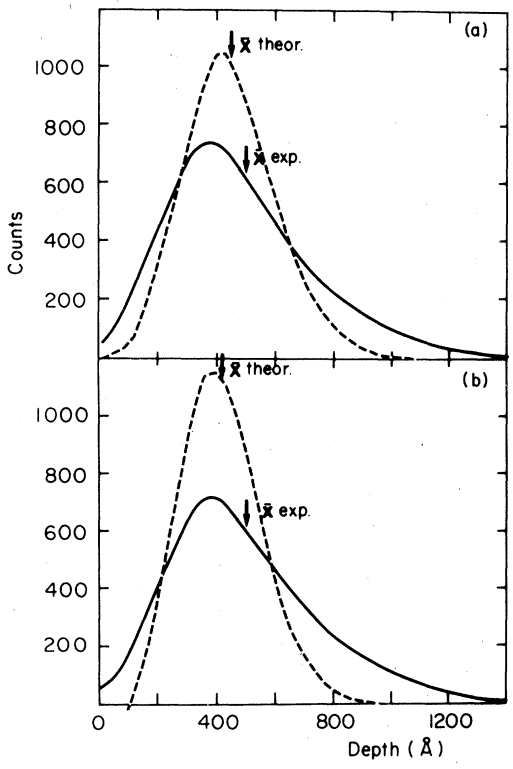

FIG. 4. Comparison between experimental (full lines) and theoretical (dashed lines) depth profiles of Yb and Au ions implanted at 400 keV in a random direction in iron.

TABLE I. Moments of the range distribution of Yb and Au ions implanted in iron at 400 keV in a random direction.

	Theoretical moments				Experimental moments			
	$\bar{x}$ (Å)	σ (Å)	$\bar{x}/\sigma$	μ^3/σ^3	$\bar{x}$ (Å)	σ (Å)	$\bar{x}/\sigma$	μ^3/σ^3
*Fe*Yb (400 keV)	446	154	2.896	0.373	500	255	1.961(78)	0.765(92)
*Fe*Au (400 kev)	417	139	3.0	0.408	499	258	1.934(77)	0.354(43)

duced moments are listed in Table I. The projected range $\bar{x}$ of the experimental profiles is in good agreement with the predicted $\bar{x}$. However the experimental variance and skewness (characteristic of the profile asymmetry) are much higher than predicted, the discrepancy being significantly greater than usually observed for implantation in amorphous or polycrystalline materials. This is likely due to "feeding in" effects induced by nuclear collisions. Some initially random Yb ions will become channeled over part of their path, thus accounting for the profile tail at large penetration depths. Similarly, the tail towards the surface is probably due to Yb ions suffering abnormally high stopping over part of their path, i.e., to ions with transverse energies of the order of the critical transverse energy for channeling (such ions are responsible for the "shoulder effects" in channeling backscattering experiments).

The profiles were found to be independent of the implantation or annealing temperature, demonstrating the absence of significant impurity migration. This point is crucial for the interpretation of the lattice-location results.

IV. RESULTS

A. Annealing behavior of room-temperature implants

The results presented in this section all relate to implantations carried out in a random direction.

1. Yb implants

The values of ϵ as a function of annealing temperature were measured for the [100], [110] axes and (100), (110) planes; the results are shown in Table II (from Ref. 8) for our 400 keV implants. Alexander *et al.*[7] found values of 0.58 at RT and 0.31 after annealing at 300 °C, for 80-keV Yb implants. We have repeated the latter experiment and found $\epsilon = 0.43 \pm 0.04$ (see I). Thus, we confirm that annealing at 300 °C reduces ϵ for a 80 keV implant, while for a 400 keV implant a reduction is only observed after annealing at or above 450 °C. For the latter annealing temperatures, the values of ϵ are higher along the (100) plane than for all other crystallo-

TABLE II. Corrected extinction ratio ϵ for the Yb impurity, and extinction ratio $(1-\chi_{Fe})$ for the Fe host at Yb depth. Iron crystals were implanted at room temperature in a random direction and then annealed up to 600 °C. Implanted dose: 5×10^{14} cm^{-2} Yb ions; implantation energy: 400 keV. Indicated uncertainties are statistical only.

Channeling	Annealing temperatures									
	No annealing		300 °C		450 °C		520 °C		600 °C	
	ϵ	$(1-\chi)_{Fe}$	ϵ	$(1-\chi)_{Fe}$	ϵ	$(1-\chi)_{Fe}$	ϵ	$(1-\chi)_{Fe}$	ϵ	$(1-\chi)_{Fe}$
[100]	0.54 ± 0.02	0.92 ± 0.01	0.56 ± 0.02	0.93 ± 0.01	0.46 ± 0.02	0.92 ± 0.01	0.16 ± 0.02	0.95 ± 0.01	0.17 ± 0.02	0.93 ± 0.01
[111]							0.14 ± 0.02	0.93 ± 0.01		
(100)	0.54 ± 0.03	0.51 ± 0.015	0.56 ± 0.03	0.45 ± 0.015	0.54 ± 0.03	0.39 ± 0.015	0.33 ± 0.03	0.48 ± 0.015	0.22 ± 0.03	0.55 ± 0.015
(110)							0.19 ± 0.03	0.70 ± 0.015		
(111)							0.14 ± 0.03	0.40 ± 0.015		

TABLE III. Corrected extinction ratio ϵ for the Au impurity, and extinction ratio $(1-\chi_{Fe})$ for the Fe host at Au depth. Iron crystals were implanted at room temperature in a random direction and then annealed at 500 °C. Implanted dose: 5×10^{14} cm^{-2} Au ions; implantation energy: 400 keV. Indicated uncertainties are statistical only.

Channeling direction	No annealing		500 °C annealing	
	ϵ	$(1-\chi)_{Fe}$	ϵ	$(1-\chi)_{Fe}$
[100]	0.81 ±0.02	0.90 ±0.01	0.94 ±0.02	0.95 ±0.01
(110)	0.82 ±0.03	0.47 ±0.015	1.01 ±0.03	0.71 ±0.015
(100)	0.80 ±0.03	0.31 ±0.015	1.00 ±0.03	0.61 ±0.015

graphic directions; below 450 °C, ϵ is the same for all the axes and planes investigated. Table II also presents the values of $1-\chi_{Fe}$ averaged over the depth interval corresponding to the profile of the implanted Yb. These values are related to the "disorder" of the crystal in the implanted region, and strong variations are observed for the (100) direction when the annealing temperature is increased. Values of ϵ above 500 °C were checked repeatedly in separate experiments for all the investigated directions: no value smaller than 0.15 was found at 600 °C.

We have compared angular scans across the [100] axis as well as the (100) and (110) planes, for Fe and Yb (Fig. 5). The full widths at half maximum $\psi_{1/2}$ of these scans are comparable (the values for Yb being about 10% smaller). As seen in Fig. 5 no significant flux peaking effect was observed on the Yb scans. This is in contrast to results obtained on Br in Fe,[17] but in agreement with other experiments[7] on Yb in Fe performed at lower implantation energies.

2. *Au implants*

The results on ϵ are reported in Table III after a 500 °C anneal; ϵ is essentially equal to 1. The values of $1-\chi_{Fe}$ at the Au-implantation depth indicate complete crystal recovery upon annealing. Spectra before and after annealing are shown in Fig. 3.

B. Hot implants

The values of ϵ and $1-\chi_{Fe}$ at the Yb depth are shown as a function of implantation temperature for various crystallographic directions in Table IV. The results are strikingly different from those of Table II.

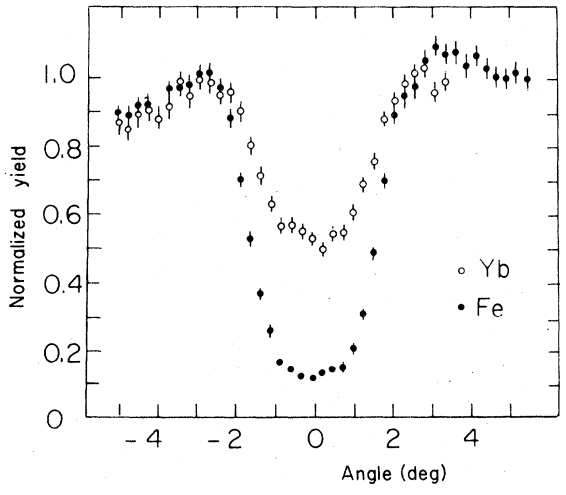

FIG. 5. Typical angular scan across the [100] axis for Fe host (full circles) and Yb impurity (open circles). Fe crystals implanted at RT with 5×10^{14} Yb atoms/cm^2 at 400 keV.

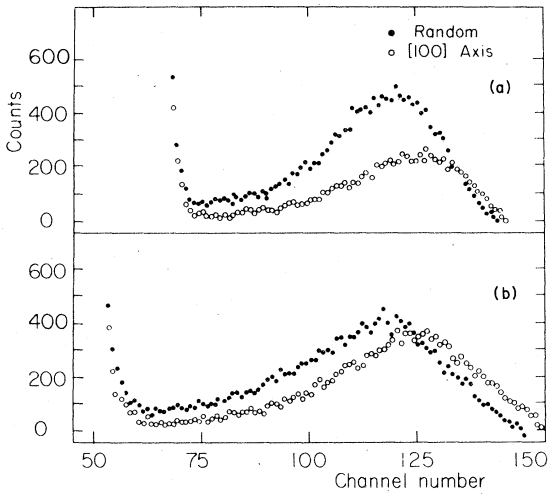

FIG. 6. Random and [100] aligned backscattering spectra on Fe crystals implanted with 5×10^{14} Yb atoms/cm^2 at 400 keV: (a) RT implantation followed by annealing at 300 °C. (b) implantation performed at 300 °C. Calibration: (a) 6.5 keV/channel, (b) 4.7 keV/ channel.

TABLE IV. Corrected extinction ratio ϵ for the Yb impurity, and extinction ratio $(1-\chi_{Fe})$ for the Fe host at Yb depth. Iron crystals were implanted at different temperatures up to 520 °C in a random direction. Implanted dose: 5×10^{14} cm^{-2} Yb ions; implantation energy: 400 keV. Indicated uncertainties are statistical only.

Channeling direction	Implantation temperatures: RT		175 °C		300 °C		400 °C		520 °C	
	ϵ	$(1-\chi)_{Fe}$	ϵ	$(1-\chi)_{Fe}$	ϵ	$(1-\chi)_{Fe}$	ϵ	$(1-\chi)_{Fe}$	ϵ	$(1-\chi)_{Fe}$
[100]	0.54 ± 0.02	0.92 ± 0.01	0.50 ± 0.02	0.93 ± 0.01	0.22 ± 0.02	0.91 ± 0.01	0.16 ± 0.02	0.89 ± 0.01	0.12 ± 0.02	0.95 ± 0.01
(110)					0.20 ± 0.03	0.54 ± 0.015	0.19 ± 0.03	0.59 ± 0.015	0.09 ± 0.03	0.65 ± 0.015
(100)	0.54 ± 0.03	0.51 ± 0.015	0.47 ± 0.03	0.47 ± 0.015	0.33 ± 0.03	0.46 ± 0.015	0.32 ± 0.03	0.45 ± 0.015	0.18 ± 0.03	0.55 ± 0.015

Specifically, ϵ is significantly reduced at an implantation temperature of 300 °C. This is illustrated in Fig. 6 which compares spectra obtained (a) after RT Yb implant followed by annealing at 300 °C and (b) after Yb implantation at 300 °C. Variations of $1-\chi_{Fe}$ with implantation temperature are also observed, particularly for the (100) plane. As in Sec. IV A, several checks were made on the values of ϵ, which were found to remain above 0.12 at 500 °C for all the directions studied.

C. Aligned Yb implants

In these experiments, 80-keV Yb ions were implanted along the [100] axis at room temperature. Figure 7 shows random and [100] aligned spectra obtained in this case. They exhibit two maxima. The lower-energy part of the spectra corresponds to Yb ions channeled over a fraction of their path and is hence related to dechanneling processes. The shape of the distributions does not allow a clear-cut analysis, but the position of the peak nearest to the surface (~180 Å) is consistent with the value obtained by assuming that this part of the distribution corresponds to unchanneled particles (whose projected range is $R_P \sim 130$ Å according to Lindhard, Scharff, and Schiott).[24]

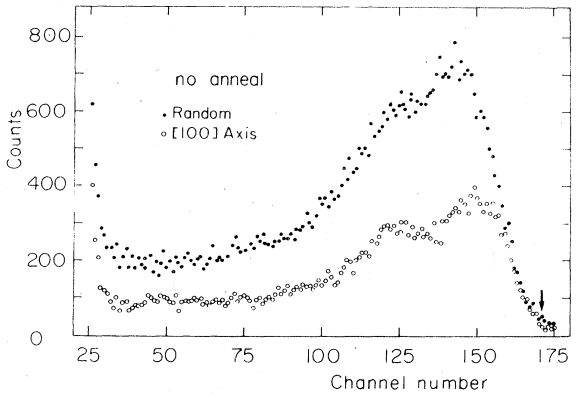

FIG. 7. Random and [100] aligned backscattering spectra obtained on an Fe crystal implanted at RT along the [100] direction with 5×10^{14} Yb atoms/cm^2 at 80 keV. Calibration: 4.2 keV/channel. Arrow corresponds to particles backscattered from surface Yb atoms.

In order to determine the effect of the aligned implantation on the impurity site, values of ϵ were calculated at increasing depths for the [100] axis and the (100) plane. Although the values of ϵ obtained in this way are somewhat uncertain (see Sec. III), a definite increase of ϵ with the Yb atom penetration depth was observed when the impurity range was divided into four equal parts and the corrected backscattering ratio was calculated for each section thus obtained. In the first section (average depth ~180 Å), $\epsilon = 0.53 \pm 0.03$ for all channeling directions; in the second section (average depth ~400 Å), $\epsilon = 0.58 \pm 0.03$ for the [100] axis and $\epsilon = 0.68 \pm 0.05$ for the (100) plane; in the third (~800 Å), $\epsilon = 0.61 \pm 0.05$ for the [100] axis and $\epsilon = 0.75 \pm 0.08$ for the (100) plane; in the last (~1300 Å), $\epsilon = 0.63 \pm 0.06$ for the [100] axis and $\epsilon = 0.76 \pm 0.10$ for the (100) plane.

V. DISCUSSION

The following is a very brief qualitative discussion of our main results. A quantitative analysis, based on the physics discussed here, of both the HFI results of Paper II and of the lattice-location results of Sec. IV is detailed in the next paper (see Paper IV).

A. Annealing of room-temperature-implanted *Fe*Yb

These results were partially reported[8] earlier (Table II). As discussed in Paper IV (Sec. IV) vacancies are known[25,26] to be mobile in Fe around 150 °C, while stereo electron microscopy[27] revealed that Yb implantation in Fe produces stable vacancy loops and indicated that such loops lie in the (100) planes.

The value obtained for the ratio ϵ after room-

temperature implantation (before annealing) is in agreement with previous[7] results and similar to results obtained on other heavy impurities[3,9,18,28] implanted in Fe. It may be related to lattice strain relaxation (and its possible effect on the impurity-damage interaction) as discussed in Paper IV (Sec. II).

As the annealing temperature is raised above the vacancy mobility threshold, the vacancy loops grow in their plane [the (100) plane] by vacancy trapping. This entails a reduction of $1-\chi_{Fe}$ in the (100) plane (Table II) but no change in the values of ϵ. When the temperature is high enough (~450 °C), the loops begin to anneal out by releasing vacancies. The latter may then interact with Yb impurities: the ratio ϵ decreases (this decrease is slower in the loop plane). In view of the HFI results (see Paper II) we suggest that vacancy-assisted Yb mobility leads to impurity "precipitation," preferentially in the (100) plane. As the loops anneal out, the increase of $(1-\chi_{Fe})$ in the (100) plane shows a recovery of the iron lattice (Table II). As discussed in Papers II and IV, precipitation is to be taken in a very loose sense, related to the impossibility of rare-earth ion spin alignment.

The difference between the temperature dependence of ϵ observed in the present work and measurements performed after Yb implantation at 80 keV (Ref. 7) is discussed in Paper I, in terms of an interaction between the RE impurities and the surface oxide layer when the implantation energy is low.

B. Annealing of room-temperature-implanted *Fe*Au

If the impurity lattice site—and HFI—evolutions are indeed governed by vacancy-assisted migration, it is interesting to compare soluble and nonsoluble impurities. The migration process, occurring when vacancies are released by the loops, leads to precipitation of the latter and should presumably lead to improvement of the solid solution for the former. This is confirmed by the results on Au implanted in Fe. The rather high value of the ratio ϵ after room-temperature implantation is discussed in Paper IV, where the impurity atomic radius is related to ϵ for all known implants in Fe (Sec. III).

C. High-temperature implantation of Yb in Fe

In these experiments, ϵ is reduced significantly as soon as vacancy mobility sets in; this reduction is weaker in the (100) plane than in other directions, particularly between 300 and 400 °C (Table IV). We suggest that vacancy-assisted migration is again the decisive factor, leading to Yb migration towards implantation-produced vacancy loops during the implantation process itself. At 400 °C the Fe extinction ratio $(1-\chi_{Fe})$ increases in the (100) plane, indicating lattice structure recovery (Table IV). Simultaneously, the (100)-plane value of ϵ drops, as does the impurity HFI (see Paper II). We conclude that vacancy loops are then no longer stable, so that vacancy-assisted Yb migration leads to precipitation as in Sec. V A, or to trapping by stable defects. This interpretation, as well as the constancy of HFI up to ~400 °C, is supported by the calculations of Paper IV.

ACKNOWLEDGMENTS

It is a pleasure to thank E. D'Artemare, D. Girard, F. Lalu, and M. Salomé for technical assistance in these experiments. We have benefited from discussions and correspondence with several colleagues, especially R. B. Alexander, G. Amsel, and L. C. Feldman. We are particularly indebted to A. L'Hoir for his aid in the profile calculations of Sec. III B. This work was supported by CNRS under Grant No. RCP-157.

---

*This work is part of a Ph.D. thesis submitted by L. Thomé to Université Paris-Sud.

[1]L. Thomé, H. Bernas, M. Bruneaux, C. Cohen, and J. Chaumont, Phys. Rev. B 14, 2787 (1976), hereafter called I; L. Thomé, H. Bernas, and R. Meunier, preceding paper [Phys. Rev. B 20, 1771 (1979)], hereafter called II; L. Thomé, H. Bernas, and C. Cohen, following paper [Phys. Rev. B 20, 1789 (1979), hereafter called IV.

[2]L. C. Feldman, E. N. Kaufmann, D. W. Mingay, and W. M. Augustyniak, Phys. Rev. Lett. 27, 1145 (1971).

[3]L. C. Feldman and D. Murnick, Phys. Rev. B 5, 1 (1972).

[4]E. N. Kaufmann, J. M. Poate, and W. M. Augustyniak, Phys. Rev. B 7, 951 (1973).

[5]H. de Waard and L. C. Feldman, *Applications of Ion Beams to Metals,* edited by S. T. Picraux, E. Eer Nisse, and F. Vook (Plenum, New York, 1974), p. 317.

[6]H. de Waard, Phys. Scr. 11, 157 (1975).

[7]R. B. Alexander, E. J. Ansaldo, B. I. Deutch, J. Gellert, and L. C. Feldman, Hyp. Int. 3, 45 (1977).

[8]F. Abel, M. Bruneaux, C. Cohen, H. Bernas, J. Chaumont, and L. Thomé, Solid State Commun. 13, 113 (1973); see Ref. 4, p. 377.

[9]H. de Waard, R. L. Cohen, S. R. Reintsema, and S. A. Drentje, Phys. Rev. B 10, 3760 (1974); P. T. Callaghan, P. K. James, and N. J. Stone, Phys. Rev. B 12, 3553 (1975).

[10]K. B. Winterbon, P. Sigmund, and J. B. Sanders, K. Dan. Vidensk. Selsk. Mat.-Fys. Medd. 37, 14 (1970).

[11]H. Bernas and J. Obert, Nucl. Instrum. Methods 107, 423 (1973).

[12]G. Amsel and D. Samuel, Anal. Chem. 39, 1689 (1967).

[13]J. Chaumont, F. Lalu, M. Salomé, H. Bernas, and L. Thomé, Vide Suppl. 171, 108 (1974).
[14]J. Lindhard, K. Dan. Vidensk. Selsk. Mat.-Fys. Medd. 34, 14 (1965).
[15]G. Amsel, J. P. Nadai, E. D'Artemare, D. David, E. Girard, and J. Moulin, Nucl. Instrum. Methods 92, 481 (1971).
[16]F. Abel, G. Amsel, M. Bruneaux, C. Cohen, and A. L'Hoir, Phys. Rev. B 12, 4617 (1975).
[17]R. B. Alexander, P. T. Callaghan, and J. M. Poate, Phys. Rev. B 9, 3022 (1974).
[18]P. T. Callaghan, P. Kittel, N. J. Stone, and P. D. Johnston, Phys. Rev. B 14, 3722 (1976).
[19]F. Abel, G. Amsel, M. Bruneaux, C. Cohen, D. Maurel, S. Rigo, and J. Roussel, J. Radio Anal. Chem. 16, 587 (1973).
[20]G. Amsel, C. Cohen, and A. L'Hoir, *Ion Beam Surface Analysis,* edited by O. Meyer, G. Linker, and F. Käppeler (Plenum, New York 1976), p. 963.
[21]G. Amsel, R. Bosshard, and C. Zadje, IEEE Trans. Nucl. Sci. NS-14, 1 (1967).
[22]A. L'Hoir, 3ème cycle thesis (Université Paris VII, 1975) (unpublished).
[23]L. C. Northcliffe and R. F. Schilling, Nucl. Data A 7, 233 (1970).
[24]J. Lindhard, M. Scharff, and H. E. Schiøtt, K. Dan. Vidensk. Selsk. Mat.-Fys. Medd. 33, 14 (1963).
[25]W. Glaeser and H. Wever, Phys. Status Solidi 35, 367 (1969).
[26]N. Yoshida, M. Kiritani, and F. E. Fujita, J. Phys. Soc. Jpn. 39, 170 (1975).
[27]H. Bernas, M. O. Ruault, and B. Jouffrey, Phys. Rev. Lett. 27, 859 (1971).
[28]J. R. McDonald, R. A. Boie, W. Darcey, and R. Hensler, Phys. Rev. B 12, 1633 (1975).